Freestanding crystalline YBa_{2}Cu_{3}O_{7−x} heterostructure membranes

Zhuoyu Chen, Bai Yang Wang, Berit H. Goodge, Di Lu, Seung Sae Hong, Danfeng Li, Lena F. Kourkoutis, Yasuyuki Hikita, and Harold Y. Hwang

Phys. Rev. Materials **3**, 060801 — Published 24 June 2019

DOI: 10.1103/PhysRevMaterials.3.060801

Article type: Rapid Communication

Title: Freestanding crystalline $YBa_2Cu_3O_{7-x}$ heterostructure membranes

Zhuoyu Chen[1,2,*,†], Bai Yang Wang[1,*], Berit H. Goodge[3,4], Di Lu[1,2], Seung Sae Hong[1,2], Danfeng Li[1,2], Lena F. Kourkoutis[3,4], Yasuyuki Hikita[2], Harold Y. Hwang[1,2,†]

[1]*Geballe Laboratory for Advanced Materials, Departments of Physics and Applied Physics, Stanford University, Stanford, CA 94305, USA*

[2]*Stanford Institute for Materials and Energy Sciences, SLAC National Accelerator Laboratory, Menlo Park, CA 94025, USA*

[3]*School of Applied and Engineering Physics, Cornell University, Ithaca, NY 14853, USA*

[4]*Kavli Institute at Cornell for Nanoscale Science, Ithaca, NY 14853, USA*

* These authors contributed equally to this work.
[†] Corresponding authors: zychen@stanford.edu, hyhwang@stanford.edu

Abstract

We report the synthesis of millimeter-sized freestanding single-crystal $YBa_2Cu_3O_{7-x}$ heterostructure membranes with nanoscale thickness. On a $SrTiO_3$ substrate, a heteroepitaxial water-soluble sacrificial layer of $Sr_3Al_2O_6$ followed by an encapsulated $YBa_2Cu_3O_{7-x}$ film is grown by pulsed laser deposition. A freestanding $YBa_2Cu_3O_{7-x}$ heterostructure membrane is obtained by etching the sacrificial layer. Its high crystalline quality is demonstrated via X-ray diffraction, electrical measurements, and scanning transmission electron microscopy.

I. INTRODUCTION

The advent of crystalline van der Waals two-dimensional nanomaterials has enabled exciting recent scientific and technological developments [1,2]. In particular, the ability to circumvent the conventional restrictions of thermodynamic and epitaxial compatibility in direct heterostructure growth allows a wide variety of materials to be assembled post synthesis [3–5]. With similar motivations, a number of techniques have been developed for obtaining crystalline oxide nanomembranes [6,7], with a particular emphasis on materials that cannot be easily exfoliated [8–14]. Among them, a promising direction has been the use of $Sr_3Al_2O_6$ (SAO) as an epitaxial sacrificial layer that can be dissolved in room temperature water, offering a broad approach for synthesizing membranes compatible with growth on perovskites, especially transition metal oxides hosting correlated electronic systems [15,16]. While this has been demonstrated for $SrTiO_3$ (STO) and $La_{0.7}Sr_{0.3}MnO_3$, both materials are chemically stable in pH neutral water [17,18]. It remains to be seen whether this technique can be applied to water sensitive materials. Here we address this issue by developing the synthesis of freestanding crystalline $YBa_2Cu_3O_{7-x}$ (YBCO) membranes, a prototypical high-temperature superconductor [19] that is widely used for industrial superconducting tapes. While YBCO thin films have been successfully grown using a variety of methods, the high-quality and low-cost synthesis of YBCO in flexible form is enabled by ion-beam-assisted deposition (IBAD) and rolling-assisted biaxially textured substrate (RABiTS) technologies [20,21], where a flexible metal alloy with multiple oxide buffer layers is fabricated to approximate a single crystal texture, replacing the high-cost and rigid single-crystal substrate. Our approach of synthesizing freestanding YBCO provides an alternative option to fabricate flexible films with reusable

single-crystal substrates [17]. This is achieved by utilizing two important features: 1) the use of encapsulating epitaxial $LaAlO_3$ (LAO) layers to protect the YBCO, and 2) the use of an alkaline solution to dissolve the sacrificial SAO layer such that the electronic properties of the cuprate layer are preserved despite the exposure to water. Using this method, we demonstrate the fabrication of millimeter-scale freestanding YBCO heterostructure membranes with bulk-like structural and electronic properties.

II. METHODS

The freestanding perovskite membrane technique used here builds upon the epitaxial growth and the selective water-etching of the SAO sacrificial layer [17]. The cubic unit cell (space group $Pa\bar{3}$) of SAO is shown in Fig. 1(a). The lattice constant is 15.844 Å, which matches four times the STO lattice constant to within 1.5 %. Moreover, the SAO unit cell closely resembles the 4×4×4 perovskite lattice. In Fig. 1(b), the (001)-plane projection of the SAO unit cell is juxtaposed, to correct aspect ratios, with that of 4×4 lattices of STO, LAO, and YBCO [22–24]. In addition to the apparent matching of the lattice constants, we see that the oxygen and cation sublattices of SAO resemble those of the STO/LAO/YBCO systems to within small offsets [17,22,24]. This structural similarity allows for the epitaxial growth of SAO on the STO substrate and the growth of a STO/LAO/YBCO/LAO heterostructure on SAO. After the growth, the etching and transfer process begins by attaching a polymer mechanical support to the heterostructure and submerging the entire sample into an aqueous solution. Upon the complete dissolution of the SAO layer, the heterostructure is released from the substrate. It is then lifted off from the substrate via its bonding with the mechanical support. Fig. 1(c) shows a picture of a detached encapsulated YBCO membrane transferred on Si. The membrane can be transferred to

other substrates for measurements or other integration purposes. A schematic of the liftoff and transfer process is shown in Fig. 1(d).

Specifically, the YBCO heterostructures presented here were grown on 0.5 mm thick STO (100) substrates by pulsed laser deposition using a krypton fluoride excimer laser of 248 nm wavelength. Before growth, the substrate is pre-annealed for 30 minutes at 930 ^{o}C in 5×10^{-6} Torr of oxygen to achieve a sharp step-and-terrace surface. An atomically flat surface is confirmed by the reflection high-energy electron diffraction (RHEED) pattern shown in Fig. 2(a). First, 1.2 J/cm^2 laser energy density is imaged to a spot of size 5 mm^2 to deposit a 24 nm thick layer of SAO epitaxially with 1 Hz repetition rate at 700 ^{o}C in 5×10^{-6} Torr of Ar. Next, 3 unit cells of STO and 27 unit cells of LAO are grown as buffer layers by *in situ* target exchange (with O_2 in place of Ar). The 3-unit-cell STO layer improves the crystallinity of the subsequent layers. The LAO buffer layer serves to 1) prevent possible interdiffusion of Sr, Ti, Ba, and Cu atoms among SAO, STO and YBCO layers [25], 2) reduce the lattice mismatch at the SAO-YBCO interface [17], and 3) protect the water sensitive YBCO [26,27]. A 75 nm thick YBCO layer is then deposited using a laser energy density of 1.8 J/cm^2 with spot size 2.4 mm^2 and 1 Hz repetition rate at 730 ^{o}C in 500 mTorr of O_2. A LAO capping layer of 27 unit cells is then grown (at the same temperature and oxygen pressure for thermodynamically stabilizing the grown YBCO) to form a structure with LAO layers sandwiching the YBCO layer. Assuming a negligible contribution from the 3-unit-cell STO layer, this structure minimizes the internal strains coming from the lattice mismatch. Finally, the sample is annealed *in situ* for 30 minutes at 470 ^{o}C in 700 Torr of O_2 for optimal YBCO hole doping [28].

Specular RHEED oscillations are used to monitor the deposited thickness during the low-pressure growth of the SAO, STO, and LAO buffer layers as shown in Fig. 2(f). (RHEED during the growth of the subsequent layers is inaccessible due to the high oxygen pressure used.) The thicknesses of the YBCO layer and the LAO cap layer are calibrated by the pulse counts. Note that the oscillation period of SAO corresponds to the deposition of 1/4 of the SAO unit cell, i.e. the perovskite equivalent subunit [17]. RHEED patterns showing pronounced 2D streaks are recorded at the completion of each layer as seen in Fig. 2(b), 2(c), 2(d), confirming the preservation of a flat surface during growth. In Fig. 2(e), a weak three-dimensional spotty feature is noticeable along with the dominant two-dimensional streaks. Atomic force microscopy (AFM) scans are performed to characterize the surface quality, which are shown in the Supplemental Material [29]. The surface morphology of the STO buffer layer (Fig. S1(a) [29], measured *ex situ*) exhibits atomically flat steps and terraces. After completion of all layers, rounded precipitates can be seen on top of the noticeable underlying unit cell terraces, as shown in Fig. S1(b) [29], with a root-mean-square surface roughness of 1.5 nm. The precipitates are segregations of excess elements localized at the top surface of the film, which are usually seen in YBCO films grown by laser ablation, especially in optimized films with high crystallinity and good superconducting properties [30,31].

To release this YBCO heterostructure membrane, we used a roughly 100 μm thick soft polycarbonate polymer (PPC) film for adhesion, stacked on a 2 mm thick polydimethylsiloxane (PDMS) layer as the mechanical support. The SAO layer is then etched for 1 day at room temperature with a potassium hydroxide solution of pH = 12. SAO is amphoteric and thus dissolves in basic solutions as well as in pH neutral water. The basic solution is chosen to

preserve the YBCO electronic properties during the prolonged exposure to water [26,27]. Crack formations are observed with the typical size of a continuous piece reaching > 500 μm (Fig. 1(c)). The PPC, with the freestanding heterostructure attached to it, is peeled off from the PDMS using adhesive tapes and then transferred onto a Si wafer covered with a 300 μm thick SiO_2 surface layer. Prior to measurements, the PPC is removed by annealing the transferred sample in flowing oxygen at 250 ^{o}C for 2 hours.

III. RESULTS

X-ray diffraction (XRD) is used to characterize the crystalline quality of the grown YBCO heterostructure. Fig. 3(a) shows the XRD 2θ-ω scan of a sample pre- and post-freestanding processing. Prior to releasing the membrane, strong (005) and (007) YBCO peaks are seen [the (006) peak is overshadowed by the STO substrate (002) peak] alongside clear SAO (008) and LAO (002) peaks [17,24]. The measured on-substrate YBCO *c*-axis lattice constant is 11.688 ± 0.003 Å. After transferring the freestanding membrane onto a Si wafer, all three clear YBCO peaks are observed, with the YBCO (006) peak now visible in the absence of the dominant STO (002) substrate peak. Note also the disappearance of the SAO (008) peak, which confirms the dissolution of SAO. Wide angle XRD scan of the transferred membrane is provided in the Supplemental Material Fig. S2 [29], in which the series of YBCO film peaks from (002) to (0011) are observed, indicating the preservation of the crystallinity of YBCO. The *c*-axis lattice constant in the freestanding form is 11.692 ± 0.003 Å, matching the bulk value (11.691 Å) for optimally doped single crystals within error [22,32]. Grazing incidence X-ray diffraction (GIXRD) of the freestanding YBCO heterostructure membrane on Si wafer is further performed to measure the in-plane lattice constants, which is shown in the inset of Fig. 3(a) (ϕ scan with

fixed 2θ is shown in Fig. S3 [29]). A double-peak feature is observed in the 2θ-ω scan, indicating the existence of twinning of the freestanding YBCO film. The *a*-axis and *b*-axis lattice constants are found to be 3.87 ± 0.01 Å and 3.83 ± 0.01 Å, respectively, matching the values of *a* (= 3.886 Å) and *b* (= 3.820 Å) of a detwinned bulk single crystal [22].

Four-point resistivity measurements were performed to characterize the electrical properties of the YBCO membrane pre- and post-processing. To make electrical contacts, the top surface of the membrane is mechanically scored in the electrode regions to remove the LAO cap and expose the YBCO layer. Subsequently, electrodes consisting of 30 nm thick Ag and 20 nm thick Au are patterned onto the film using masked evaporation. The resistivity-versus-temperature (ρ-T) measurements for the as-grown on-substrate heterostructure and in the freestanding form on the Si wafer are shown in Fig. 3(b) upper and lower panels, respectively. An optical image of the freestanding YBCO membrane measurement configuration is shown in the inset. The two measurements showed similar ρ-T dependence with a small room-temperature ρ difference. This difference is within the error from the estimation of the geometric aspect ratio for different samples due to the finite size of electrical contacts and the irregular sample boundaries. Note also that the room-temperature ρ is close to 300 μΩcm, comparable to that of high-quality YBCO bulk single crystals [22,33]. The superconducting transition temperature T_C, defined as the temperature at which ρ becomes 50% of the normal state value just before the transition, is 92.2 K and 90.5 K for the on-substrate and the freestanding membranes, respectively. The transition width for both cases is less than 1 K (90%-10% ρ). For $T > T_C$, ρ is metallic and linear and extrapolates close to the origin. The linearity of ρ-T, high T_C, sharp superconducting transition,

and negligible residual resistivity confirm the high quality of both the as-grown and the freestanding YBCO heterostructure membranes [22,33].

Cross-sectional high-angle annular dark-field (HAADF) scanning transmission electron microscopy (STEM) of the freestanding YBCO heterostructure is performed to characterize the crystal and interface quality. Fig. 4(a) and Fig. S4 [29] confirm the abrupt interface between the LAO buffer layer and the YBCO layer, showing that the freestanding heterostructure is free from intermixing. A larger field-of-view image of the YBCO layer in the freestanding form, shown in Fig. 4(b), further demonstrates the high quality of the crystal, intact from the release process.

The YBCO and the buffer layer thicknesses presented here were intentionally chosen to be thick enough to enable clear XRD measurement results. We have also fabricated heterostructures with comparable electrical properties for YBCO thicknesses ranging from 20 nm to 150 nm, and LAO layers as thin as 5 unit cells, as shown in Fig. S4 [29]. However, there are two limiting aspects involved. First, the solubility of the SAO sacrificial layer is found to be sensitive to the growth conditions for the subsequent layers. We find that growth of YBCO at temperatures > 800 ^{o}C or utilization of LAO buffer layers below 3 nm thickness are adverse factors for clean SAO removal, possibly arising from the degradation of the SAO layer due to interdiffusion [25]. Second, crack formation limits the size of the obtainable continuous YBCO freestanding membranes (Fig. 1(c)). Possible origins include lattice mismatch, SAO layer thickness, and the intrinsic brittleness of the oxide layers. While the combination of the STO and LAO buffer layers serves to reduce the lattice mismatch with YBCO [22], and the STO layer improves the surface flatness for subsequent growth of YBCO (Fig. S1(a) [29]), there remains room for improvement

of the heterostructure design. Nevertheless, within the structural design and growth conditions reported here, > 500 μm size freestanding YBCO heterostructure membranes can be consistently produced.

In order to investigate the long-term aging phenomena of the YBCO heterostructure, we performed two degradation studies. First, to confirm the passivation effect of the LAO capping layer, we compared a capped YBCO heterostructure sample against an un-capped YBCO thin film sample on substrate. The degradation of these two samples from a 25-day exposure to atmosphere is shown in Fig. S5 [29]. While the room temperature resistance of the un-capped sample increased by about 27%, only a 7% increase is observed for the capped heterostructure, suggesting the passivation of the YBCO layer by the LAO capping layer. Second, to characterize the long-term degradation of the structure, we performed a STEM-EELS study of a freestanding heterostructure after 1-year storage in air (Fig. S6 [29]). The result shows that the LAO capping layer has become non-crystalline and a decrease of lattice quality can be seen in the top part of the YBCO layer while the rest of the film remains structurally and chemically intact. This implies that the effectiveness of the capping layer is a major factor for sample degradation.

One advantage of this freestanding technique is that the STO substrate is reusable [17]. Furthermore, the current method is readily scalable by depositing metal layers (e.g. Au, or Ag/Cu) directly on top of the YBCO instead of the LAO capping layer, which does not need to be removed afterwards since Au/Ag serves as an Ohmic contact to YBCO. For example, we have experimentally found that a thin deposited top Au metal layer (~20 nm) in place of the LAO cap layer is effective in increasing the size of the continuous membranes to the scale of the substrates

used for our investigations (> 3 mm). Moreover, the pulsed laser deposition growth technique is compatible with adding artificial pinning centers *in situ* for higher critical currents in magnetic field [20,21,34]. Thus, our results may provide opportunities towards further development of superconducting components for industrial applications.

IV. CONCLUSIONS

In conclusion, we have demonstrated the epitaxial growth of high-quality single-crystal encapsulated YBCO heterostructures, on top of the water-soluble epitaxial sacrificial layer SAO. Using a basic potassium hydroxide solution, we can release flexible YBCO heterostructure membranes from reusable substrates. By comparing structural and resistivity characterizations before and after the release of the freestanding YBCO heterostructure membranes, we confirm that high crystalline and electronic quality is preserved during the freestanding procedure, matching bulk values. These results should enable the incorporation of this high temperature superconductor in various composite structures post synthesis.

Acknowledgements

Zhuoyu Chen and Bai Yang Wang contributed equally to this work. This work was supported by the Department of Energy, Office of Basic Energy Sciences, Division of Materials Sciences and Engineering, under contract DE-AC02-76SF00515. Partial support was provided by the Stanford Graduate Fellowship in Science and Engineering (Z.C.), and the Gordon and Betty Moore Foundation's EPiQS Initiative through Grant GBMF4415 (electrical measurements). Part of this work was performed at the Stanford Nano Shared Facilities (SNSF). B.H.G. and L.F.K. acknowledge support from the Department of Defense Air Force Office of Scientific Research

(No. FA 9550-16-1-0305). This work made use of the Cornell Center for Materials Research (CCMR) Shared Facilities, which are supported through the NSF MRSEC Program (No. DMR-1719875). The FEI Titan Themis 300 was acquired through No. NSF-MRI-1429155, with additional support from Cornell University, the Weill Institute, and the Kavli Institute at Cornell.

References

[1] A. H. Castro Neto, F. Guinea, N. M. R. Peres, K. S. Novoselov, and A. K. Geim, Rev. Mod. Phys. **81**, 109 (2009).
[2] S. Manzeli, D. Ovchinnikov, D. Pasquier, O. V Yazyev, and A. Kis, Nat. Rev. Mater. **2**, 17033 (2017).
[3] A. K. Geim and I. V Grigorieva, Nature **499**, 419 (2013).
[4] D. Jariwala, T. J. Marks, and M. C. Hersam, Nat. Mater. **16**, 170 (2017).
[5] P. Ajayan, P. Kim, and K. Banerjee, Phys. Today **69**, 38 (2016).
[6] R. E. Schaak and T. E. Mallouk, Chem. Mater. **14**, 1455 (2002).
[7] M. Osada and T. Sasaki, Adv. Mater. **24**, 210 (2012).
[8] Q. Gan, R. A. Rao, C. B. Eom, J. L. Garrett, and M. Lee, Appl. Phys. Lett. **72**, 978 (1998).
[9] H. Ohta, A. Mizutani, K. Sugiura, M. Hirano, H. Hosono, and K. Koumoto, Adv. Mater. **18**, 1649 (2006).
[10] K.-I. Park, S. Xu, Y. Liu, G.-T. Hwang, S.-J. L. Kang, Z. L. Wang, and K. J. Lee, Nano Lett. **10**, 4939 (2010).
[11] L. Pellegrino, N. Manca, T. Kanki, H. Tanaka, M. Biasotti, E. Bellingeri, A. S. Siri, and D. Marré, Adv. Mater. **24**, 2929 (2012).
[12] D. M. Paskiewicz, R. Sichel-Tissot, E. Karapetrova, L. Stan, and D. D. Fong, Nano Lett. **16**, 534 (2016).
[13] C.-I. Li, J.-C. Lin, H.-J. Liu, M.-W. Chu, H.-W. Chen, C.-H. Ma, C.-Y. Tsai, H.-W. Huang, H.-J. Lin, H.-L. Liu, P.-W. Chiu, Y.-H. Chu, C.-I. Li, J.-C. Lin, H.-J. Liu, M.-W. Chu, H.-W. Chen, C.-H. Ma, C.-Y. Tsai, H.-W. Huang, H.-J. Lin, H.-L. Liu, P.-W. Chiu, and Y.-H. Chu, Chem. Mater. **28**, 3914 (2016).
[14] S. R. Bakaul, C. R. Serrao, M. Lee, C. W. Yeung, A. Sarker, S. Hsu, A. K. Yadav, L. Dedon, L. You, A. I. Khan, J. D. Clarkson, C. Hu, R. Ramesh, and S. Salahuddin, Nat. Commun. **7**, 10547 (2016).
[15] H. Takagi and H. Y. Hwang, Science **327**, 1601 (2010).
[16] H. Y. Hwang, Y. Iwasa, M. Kawasaki, B. Keimer, N. Nagaosa, and Y. Tokura, Nat. Mater. **11**, 103 (2012).
[17] D. Lu, D. J. Baek, S. S. Hong, L. F. Kourkoutis, Y. Hikita, and H. Y. Hwang, Nat. Mater. **15**, 1255 (2016).
[18] S. Sae Hong, J. Ho Yu, D. Lu, A. F. Marshall, Y. Hikita, Y. Cui, and H. Y. Hwang, Sci. Adv. **3**, eaao5173 (2017).
[19] B. Keimer, S. A. Kivelson, M. R. Norman, S. Uchida, and J. Zaanen, Nature **518**, 179

(2015).
[20] S. R. Foltyn, L. Civale, J. L. Macmanus-Driscoll, Q. X. Jia, B. Maiorov, H. Wang, and M. Maley, Nat. Mater. **6**, 631 (2007).
[21] X. Obradors and T. Puig, Supercond. Sci. Technol. **27**, 044003 (2014).
[22] R. Liang, P. Dosanjh, D. a. Bonn, D. J. Baar, J. F. Carolan, and W. N. Hardy, Phys. C Supercond. **195**, 51 (1992).
[23] K. Momma and F. Izumi, J. Appl. Crystallogr. **44**, 1272 (2011).
[24] S. A. Hayward, F. D. Morrison, S. A. T. Redfern, E. K. H. Salje, J. F. Scott, K. S. Knight, S. Tarantino, A. M. Glazer, V. Shuvaeva, P. Daniel, M. Zhang, and M. A. Carpenter, Phys. Rev. B **72**, 054110 (2005).
[25] T. Nakamura and M. Iiyama, Jpn. J. Appl. Phys. **34**, 4765 (1995).
[26] R. L. Barns and R. A. Laudise, Appl. Phys. Lett. **51**, 1373 (1987).
[27] M. F. Yan, R. L. Barns, H. M. O'Bryan, P. K. Gallagher, R. C. Sherwood, and S. Jin, Appl. Phys. Lett. **51**, 532 (1987).
[28] T. Haugan, P. N. Barnes, L. Brunke, I. Maartense, and J. Murphy, Phys. C Supercond. **397**, 47 (2003).
[29] See Supplemental Material at [URL will be inserted by publisher] for more details.
[30] J. P. Gong, M. Kawasaki, K. Fujito, R. Tsuchiya, M. Yoshimoto, and H. Koinuma, Phys. Rev. B **50**, 3280 (1994).
[31] N. Kanda, M. Kawasaki, T. Kitajima, and H. Koimuma, Phys. Rev. B **56**, 8419 (1997).
[32] R. Liang, D. A. Bonn, and W. N. Hardy, Phys. Rev. B **73**, 180505(R) (2006).
[33] R. Wördenweber, Supercond. Sci. Technol. **12**, R86 (1999).
[34] T. Haugan, P. N. Barnes, R. Wheeler, F. Meisenkothen, and M. Sumption, Nature **430**, 867 (2004).

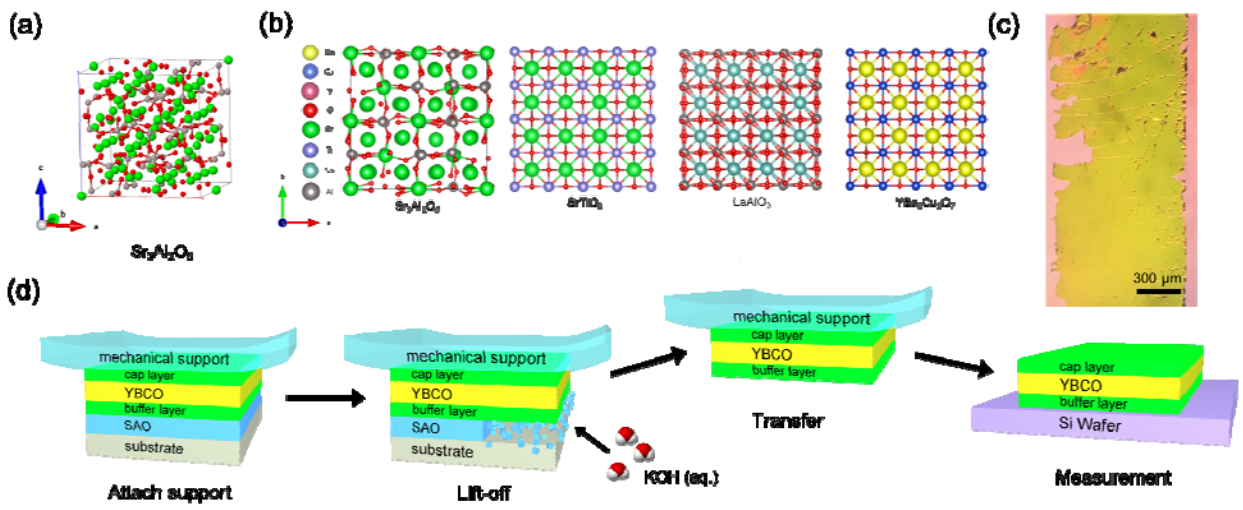

FIG. 1. (a) Unit cell of $Sr_2Al_3O_6$. (b) Juxtaposition of scaled ab-plane projections of half of a SAO unit cell, 4×4 STO unit cells, 4×4 LAO pseudo-cubic unit cells, and 4×4 YBCO unit cells (Y is overshadowed by Ba). (c) Optical image of a typical freestanding LAO-encapsulated 75 nm thick YBCO heterostructure on PPC/PDMS with millimeter-sized continuous pieces. (d) Schematic diagram of the processing steps to release the heterostructure.

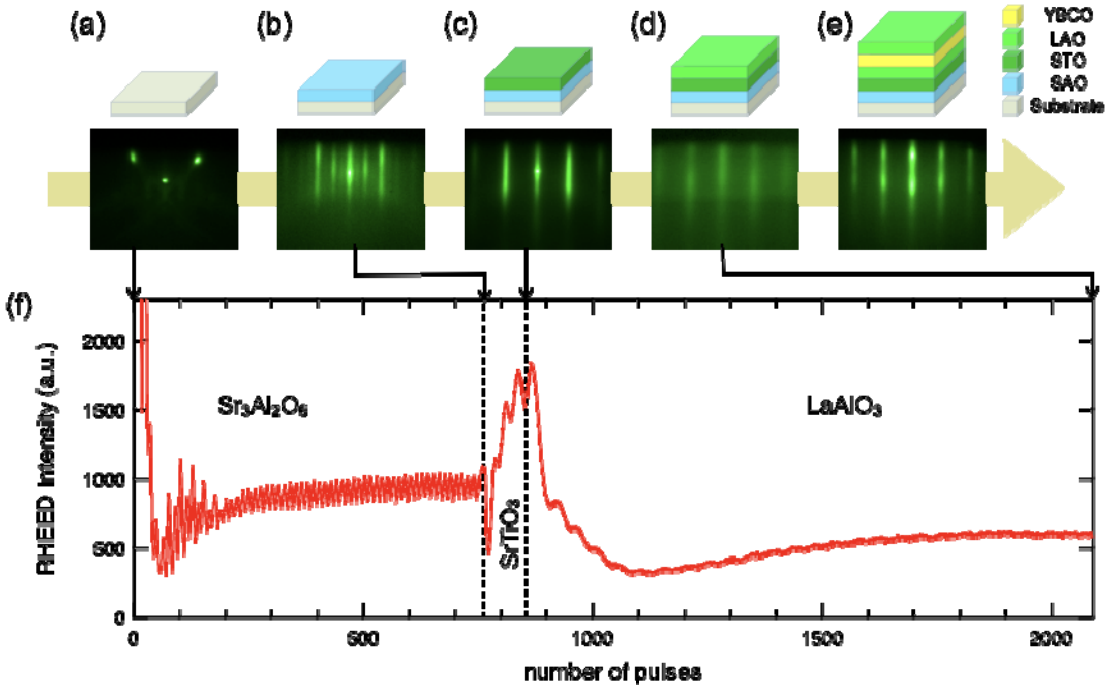

FIG. 2. (a-e) RHEED patterns along the substrate {100} direction upon the completion of the growth of each layer. The schematics above the RHEED patterns illustrate the structures of the sample at each corresponding stage. The substrate is STO (100). (f) RHEED oscillations for the low-pressure growth of the sacrificial layer and the buffer layers. The dashed lines indicate pauses during the growth for switching targets and tuning the growth conditions. RHEED intensities are normalized to match at the dashed lines. The RHEED oscillations for the first 2 unit cells of SAO are partly cropped by the intensity limit.

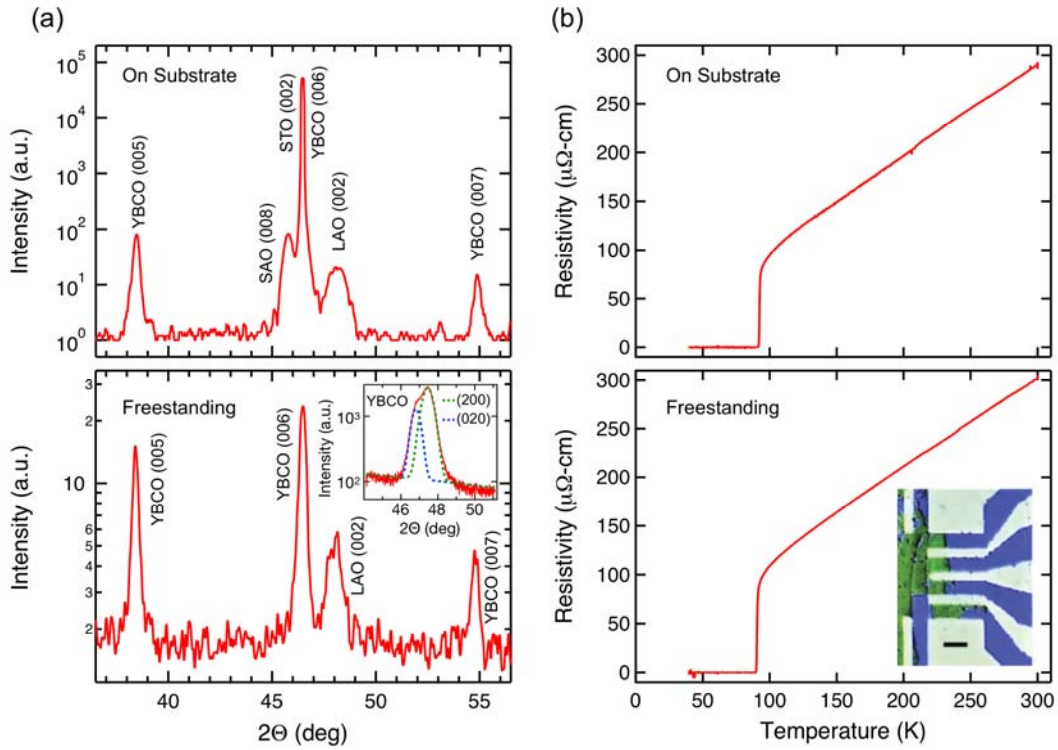

FIG. 3. (a) 2θ-ω XRD scan of the YBCO heterostructure before (upper panel) and after (lower panel) liftoff. For the upper and lower panels, the 2θ axes are calibrated by the STO (002) peak and Si (004) peak, respectively. In the upper panel, the YBCO (006) peak is overshadowed by the STO (002) peak. The inset of the lower panel shows the 2θ-ω GIXRD scan for the freestanding YBCO heterostructure. Blue and green curves are fits for the two resolved peaks in the scan, from which the YBCO lattice constants along *a* and *b* axes are extracted respectively. (b) Resistivity-versus-temperature measurement of the YBCO heterostructure before (upper panel) and after (lower panel) liftoff. Inset: four-probe resistivity measurement configuration. The scale bar is 100 μm long.

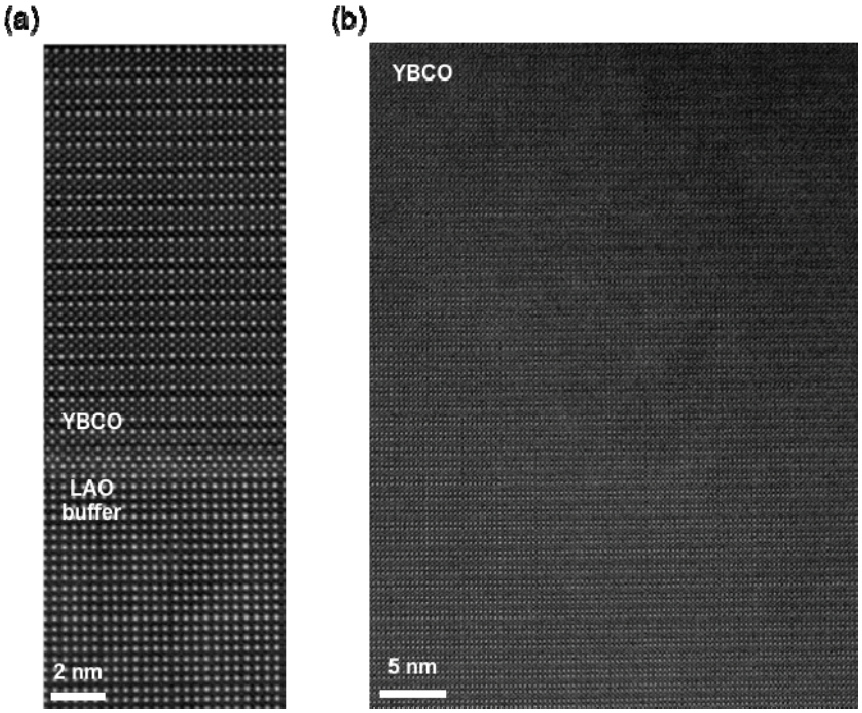

FIG. 4 Cross-sectional HAADF STEM images of (a) the interface between the YBCO layer and the LAO buffer layer in the {100} direction and (b) a larger field-of-view of the YBCO layer of the transferred freestanding heterostructure on a Si wafer.